



Vortex Ring Formation Following Shock Wave Diffraction in Low-Pressure Environments

Ziqu Cao¹ · Konstantinos Kontis¹ · Hamid Hosano² · Craig White¹ · Ting-Tsung Chang¹ · Muhammed Burak Agir³

Received: 7 March 2023 / Accepted: 28 August 2023 / Published online: 9 September 2023
© The Author(s) 2023

Abstract

Compressible vortex rings have been widely investigated for decades under ambient atmospheric conditions, and understanding this transient phenomenon is important for improving the thrust vector and avoiding surface impingement and contamination. However, how the vortex ring behaves in a reduced pressure environment remains unknown. This work provides schlieren imaging and pressure measurement results of the vortex ring when the environmental pressure is lower than 1 atm. The basic structure of the compressible vortex ring in low-pressure environments has been captured. The reduced environmental pressure will degenerate the internal flow structure, including the shock wave, the CRVRs, and the vortices due to the Kelvin–Helmholtz instability, which is consistent with the conclusion of previous numerical work. The vortex ring is confirmed to exist when the environmental pressure is approximately 1.0 kPa.

Keywords Compressible vortex ring · Shock tube · Low-pressure

✉ Ziqu Cao
caoziqu@qq.com

Konstantinos Kontis
kostas.kontis@glasgow.ac.uk

Hamid Hosano
hamid@kumamoto-u.ac.jp

Craig White
craig.white.2@glasgow.ac.uk

Ting-Tsung Chang
2591603C@student.gla.ac.uk

Muhammed Burak Agir
muhammed.agir@strath.ac.uk

¹ James Watt School of Engineering, University of Glasgow, Glasgow G12 8QQ, UK

² Department of Biomaterials and Bioelectronics, Institute of Industrial Nanomaterials, Kumamoto University, Kumamoto 860-8555, Japan

³ Department of Naval Architecture, Ocean and Marine Engineering, University of Strathclyde, Glasgow G4 0LZ, UK

1 Introduction

Compressible vortex rings, as a common phenomenon in aerospace engineering, have been studied intensively for decades, both experimentally and numerically, in the atmosphere (Elder and De Haas 1952; Baird 1987; Hillier 1991; Brouillette and Hebert 1997; Kontis et al. 2006; Murugan et al. 2012; Dora et al. 2014; Zhang et al. 2014; Poudel et al. 2021). Understanding compressible vortex ring evolution is fundamental to thrust control improvement (Cao et al. 2021) and avoiding contamination and impingement on sensitive surfaces (Martinez and Worthy 2020). In our previous work (Cao et al. 2021), vortex loop formation due to shock wave diffraction under rarefied conditions was numerically investigated using the direct simulation Monte Carlo (DSMC) method. It is noticed that the shock wave and the vortex strength are reduced with an increase in the Knudsen number, Kn , which is the ratio of the mean free path of the gas, λ to a characteristic length scale, L . The existence of shock wave diffraction and the formation of the vortex loop in the near continuum ($Kn \approx 0.001$), slip, and transition flow regimes ($0.001 < Kn < 10$) are observed through the simulation. The failure of the vortex loop formation is found in the free-molecular flow regime ($Kn > 10$), which implies a trend that the vortex ring gradually degenerates as the environmental pressure decreases and eventually fails to form when the environmental pressure is reduced to the free-molecular flow regime. However, no relevant proof has been reported, and experimental evidence is of great importance. Studying the compressible vortex ring in low-pressure conditions is helpful to understand the vortex mechanism and evaluate the significance of the vortex in a low-pressure environment, but how the vortex ring evolves in a low-pressure environment becomes a knowledge gap. If the vortex degeneration trend in rarefied conditions found in previous numerical work holds (Cao et al. 2021), it should be able to be observed when the environmental pressure decreases.

A vortex ring is usually generated by a shock tube in laboratory experiments. Shock tubes are a facility capable of producing both high pressure and high temperature jumps in a short time (Bradley 1963). A typical shock tube is separated into two parts by a diaphragm: the driver section, which contains high-pressure gas, and the driven section, which contains low-pressure gas. When the diaphragm ruptures, a discontinuity is produced, and the high-pressure gas in the driver section expands into the driven section, resulting in the formation of a shock wave and an expansion wave that are transmitted to the driven and driver tubes, respectively (Li et al. 2019). When the shock tube is opened, shock wave diffraction occurs at the exit and a vortex ring forms subsequently, followed by the formation of a series of internal structures, such as embedded shock waves (Elder and De Haas 1952) and a counter-rotating vortex ring (CRVR) (Thangadurai and Das 2010; Dora et al. 2014) in front of the primary vortex ring. To observe compressible vortex rings, the basic optical techniques including schlieren, particle image velocimetry, and planar laser-induced fluorescence have been extensively used in ambient atmosphere environments but have never been applied to the visualisation of compressible vortex rings or loops in reduced pressure conditions.

This work aims to investigate the vortex ring in a low-pressure environment at a fundamental level. The specific objectives of this work are to study the variation of the internal structure of the vortex ring when the environmental pressure is reduced, to look for experimental evidence of the trend of vortex degeneration, and to experimentally prove the qualitative results of our previous numerical work.

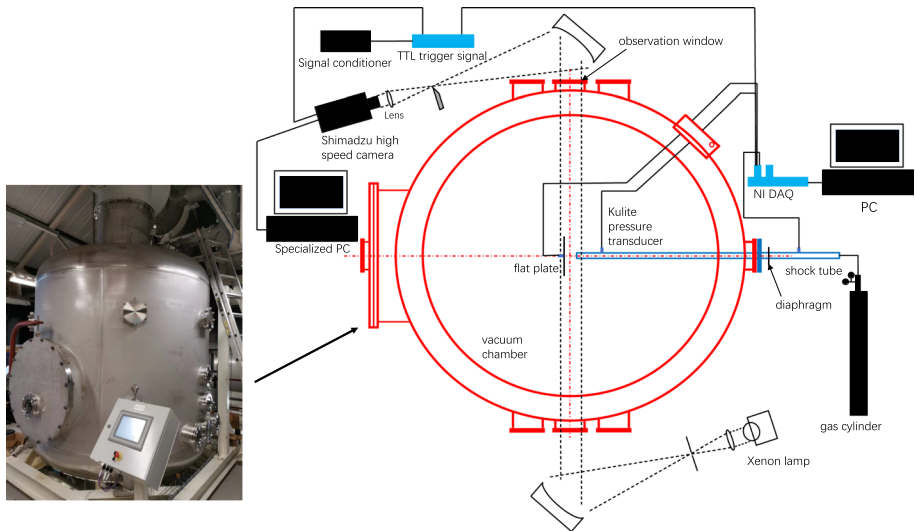


Fig. 1 Schematic of the experimental layout

2 Experimental Apparatus

2.1 Shock Tube Design Detail

The open-ended shock tube is manufactured using standard parts. The small flanges between the tubes are KF40 type vacuum flanges and are sealed with aluminium clamps. The outer diameter of the tube is 25 mm and the inner diameter, denoted D , is 20 mm. The connector is machined based on an ISO200 blank flange and it is used to connect the shock tube to the vacuum chamber. The lengths of the driver and driven sections are 742×1405.7 mm, corresponding to $37D$ and $70D$, respectively. The length of the driven section is much longer than the recommended minimum length ($8D-10D$) (Bradley 1963) and is sufficient to allow for shock wave formation. The lengths of the driver and driven sections are variable by adding or subtracting tubes. 20 micron thick aluminium foil is used as a diaphragm and is placed at the flange connection between the vacuum flange and driver part. The feasibility of the shock tube must be validated before any further improvements are considered, so no diaphragm-breaking system, such as that in the work of Qin et al. (2020) and Xiang et al. (2023), is added in the current work; the diaphragm is broken naturally through the pressure difference between the driver and the driven sections. The design and use of a diaphragm-breaking system is considered to be future work.

2.2 Experimental Setup

The experiment layout is presented in Fig. 1. The red line is the cross-section of the vacuum chamber, with an outer diameter of 2.52 m and a volume of 12 m^3 (White et al. 2019). This vacuum chamber is connected to a 60 m^3 buffer tank to limit the pressure

increase (i.e. during the addition of any mass) to a negligible level (White et al. 2019). The shock tube is connected at a flange opposite the access door to the chamber.

Two Kulite XTE-190 M pressure transducers were used, one each in the driver and driven sections, in order to collect pressure signals for calculating the pressure ratio. The pressure signal was recorded using an NI-9223 module (National Instruments Corp., 1 MS/s, 16 bit, 4 channels) with a NI-9178 compact data acquisition system controlled by LabVIEW. A sampling rate of 100 kHz was chosen in order to obtain high-frequency results. The combination of the Kulite XTE-190 M and the NI-9223 model provides a resolution of approximately 700 Pa.

The schlieren imaging technique is used because the experiment is still in the continuum flow regime and far outside the rarefied flow regimes (i.e. $Kn \ll 0.001$). As shown in Fig. 1, a typical Z-type schlieren system is used. The system consists of a 450–1000 W continuous light source with a Xenon arc lamp (Newport, model: 66921), a pair of 203.3 mm diameter parabolic mirrors with a focal length of 1829 mm, a knife edge to block part of the light, and a Shimadzu high-speed camera (model: HPV-1). The sudden pressure rise signal induced by the primary shock wave is used as a trigger to the camera. A signal conditioner was used to adjust the output voltage from the transistor-transistor logic trigger signal since the over pressure signal changes with the pressure inside the vacuum chamber. The limit of the environmental pressure for this schlieren system to provide useful images will be found in this work. To acquire more information beyond this limit, a flat plate with a pressure transducer at its centre is placed in front of the shock tube, inclined normal to the shock tube exit. The distance between the shock tube exit and the flat plate is 55 mm. The experimental matrix is presented in Table 1.

Conventionally, in shock tube theory, the environmental pressure or the pressure in the driven section is denoted as p_1 and the pressure in the driver section is p_4 . p_2 and p_3 are the pressures after the primary shock wave and the expansion wave inside the shock tube, respectively (Anderson 1990). In this work, we continue to use these pressure designations.

2.3 Image Processing

Background noise and contamination on the lens, mirrors or camera sensors are usually inevitable on schlieren images, giving rise to difficulties in the recognition of flow structures. It is known that background image subtraction in the frequency domain is effective in eliminating the noise (Li 2020). The image processing method and the corresponding code based on Matlab and image processing toolbox have been detailed in

Table 1 Experimental matrix

Environmental pressure p_1	Free-expansion	Flow impingement
1 bar	✓	✓
0.556 bar		✓
0.487 bar		✓
0.36 bar	✓	
0.2 bar	✓	✓
0.184 bar		✓
0.01 bar		✓

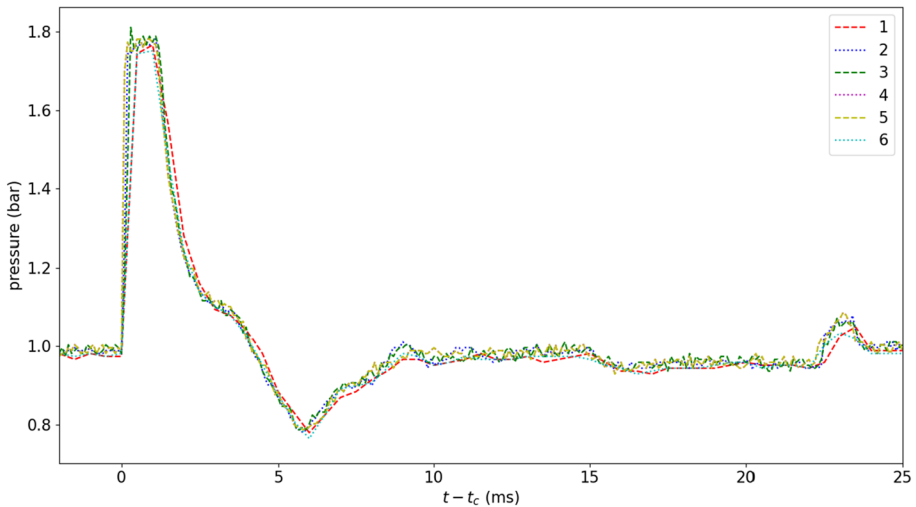


Fig. 2 Pressure signals acquired from the pressure transducer in the driven section due to the passing of the shock wave with a background pressure, p_1 , of 1 bar

Ref. Li (2020) and they will not be repeated here. All the schlieren images in this work are processed using background image subtraction in the frequency domain.

3 Repeatability Validation

To validate the shock tube repeatability, pressure measurements with a background pressure, p_1 , of 1 bar of the passing of the shock wave in the driven section were repeated 6 times using a diaphragm of aluminium foil with a thickness of 20 microns. Without changing the lengths of the driver and driven sections, the pressure distribution acquired from the transducer should be consistent. Since there is no diaphragm-breaking system in the shock tube, the diaphragm will naturally break due to rising pressure in the driver section, and the time at which the diaphragm breaks is different between runs. Thus, the time when the pressure begins to rise, denoted t_c , is considered as a reference time. Figure 2 shows the pressure variation caused by the shock wave passing through the shock tube. The average over pressure is approximately 1.78 bar, corresponding to a shock Mach number of around 1.3 in the atmosphere conditions. The average pressure ratio at which the diaphragm failed p_4/p_1 was $3.485 \pm 2.5\%$. In general, a high degree of repeatability can be found, indicating that the shock tube operates in a reliable manner when the environmental pressure p_1 is constant. As p_1 decreases, $p_4 - p_1$ and the pressure signal acquired in the driven section also change because of the force on the diaphragm due to higher $p_4 - p_1$ before pressurizing the driver section and this continuous force reduces the strength of the diaphragm, causing earlier failure of the diaphragm and lower pressure in the driver section. However, the variation of $p_4 - p_1$ when p_1 decreases does not influence the subsequent results because the flow studied in this work is still in the continuum regime and the vortex ring highly depends on the pressure ratio p_4/p_1 , which will be discussed later.

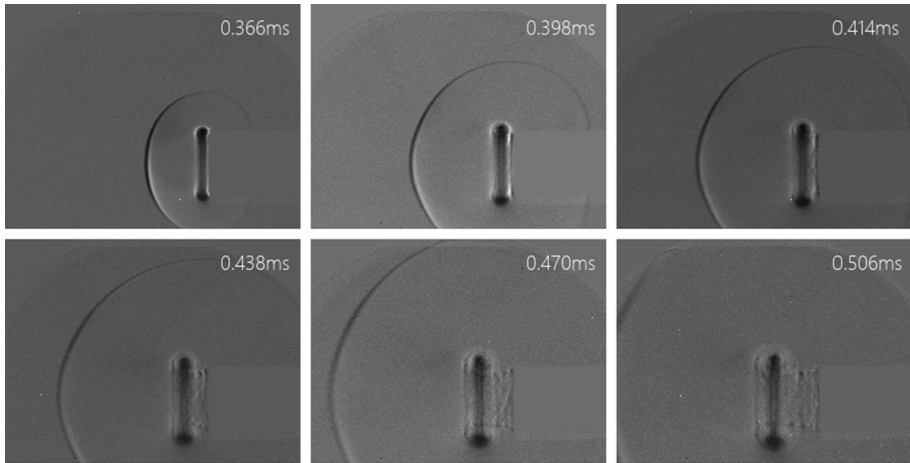


Fig. 3 Schlieren with $p_1 = 1 \text{ atm}$. $p_4/p_1 = 4.2$, corresponding to a shock Mach number of 1.37

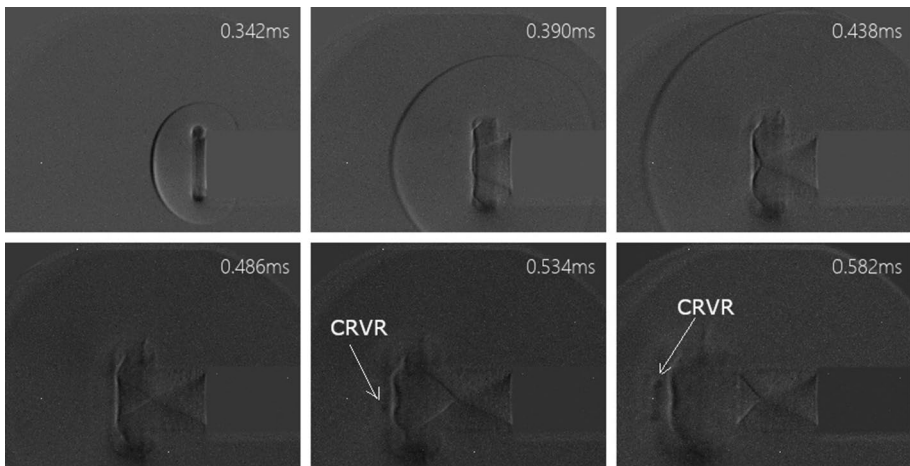


Fig. 4 Schlieren with $p_1 = 0.36 \text{ bar}$. $p_4/p_1 = 8.8$, corresponding to a shock Mach number of 1.57

4 Results and Discussions

Figures 3, 4, and 5 show the schlieren images with representative structures with environmental pressures, p_1 , equal to 1 bar, 0.36 bar, and 0.2 bar, respectively. The pressure ratio, p_4/p_1 , tends to infinity as the environmental pressure is decreased to near vacuum. The three free-expansion cases have pressure ratios of 4.2, 8.8, and 15.8, corresponding to shock Mach numbers of 1.37, 1.57, and 1.75, respectively.

In all cases, shock wave diffraction occurs at the shock tube exit, followed by separation and rolling up of the flow and finally a vortex ring forms at the nozzle lip: Figs. 3 (0.366 ms), 4 (0.342 ms), and 5 (0.104 ms). The primary shock wave becomes spherical, and the vortex ring leaves the nozzle exit and grows: Figs. 3 (0.414 ms), 4 (0.390 ms), and 5 (0.120

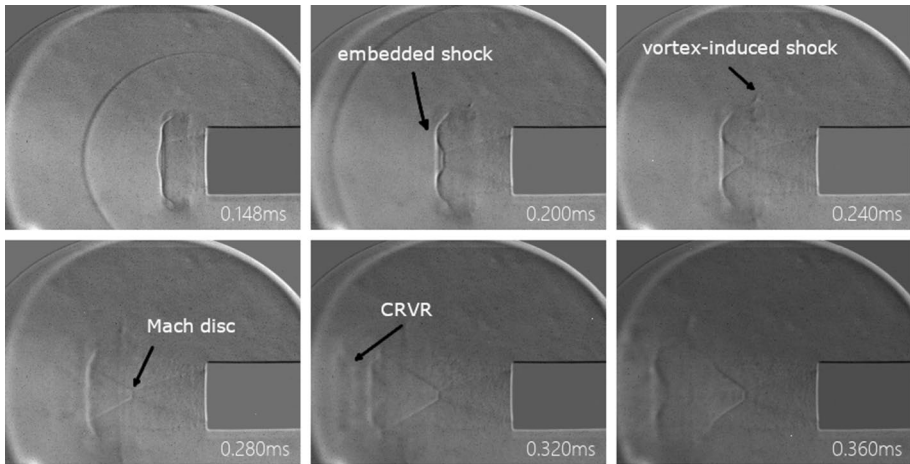


Fig. 5 Schlieren with $p_1 = 0.2$ bar. $p_4/p_1 = 15.8$, corresponding to a shock Mach number of 1.75

ms). Small vortices are formed in the shear layer and the vortex rings become turbulent because of the instability waves around the circumference of the vortex ring: Figs. 3 (0.470 ms), 4 (0.486 ms), and 5 (0.232 ms). The small vortices in the shear layer continuously feed vorticity into the primary vortex ring, helping the vortex ring to grow in size with time.

As the shock Mach number is less than 1.4, the structure of the vortex ring in Fig. 3 is shock-free, as has been confirmed in Ref. Brouillette and Hebert (1997). The flow structures, including the embedded shock wave and the x-shape oblique shock waves that can be seen in Fig. 4 are very similar to those in Figure 5 of Ref. Kontis et al. (2006).

As the pressure ratio increases, the embedded shock waves inside the vortex ring (0.39 ms in Fig. 4 and 0.2 ms in Fig. 5) occur and the joint of the oblique shock waves at 0.486 ms in Fig. 4 becomes a small Mach disc in Fig. 5 at 0.2 ms. A vortex induced shock can be clearly found at 0.438 ms and 0.486 ms in Fig. 4 and 0.232 ms in Fig. 5. In comparison with the vortex induced shock at 0.486 ms in Fig. 4, it approximately tripled its length at 0.582 ms and a similar phenomenon can also be found in Fig. 5. It is interesting that CRVRs appear when the environmental pressure is 0.36 bar and 0.2 bar. CRVR is interpreted as a result of a Kelvin–Helmholtz type instability of the vortex sheet (Zare-Behtash et al. 2008; Thangadurai and Das 2010)/slipstream beginning from the triple point of the Mach disc and following vortex coupling (Dora et al. 2014), which was supported by the numerical results from Zhang et al. (2014). These typical structures can be produced by increasing the pressure of the driver section, but they can also be produced by decreasing the pressure in the environment, as long as the pressure ratio reaches the critical value and the environment is in the continuum flow regime.

Intuitively, the flow structures in Figs. 4 and 5 become unclear as the vortex ring propagates. First, the CRVR are not as apparent as those in the atmosphere, such as the schlieren images in Figure 5 in Ref. Kontis et al. (2006) and numerical results in Ref. Zhang et al. (2014). Second, the vortex induced shock becomes weak and difficult to recognise at 0.582 ms in Fig. 4 and 0.36 ms in Fig. 5. In the atmosphere environment, a higher shock Mach number gives rise to a stronger embedded shock wave, but the shock wave thickness in schlieren images show that the embedded shock wave in Fig. 5 is weaker than that in Fig. 4.

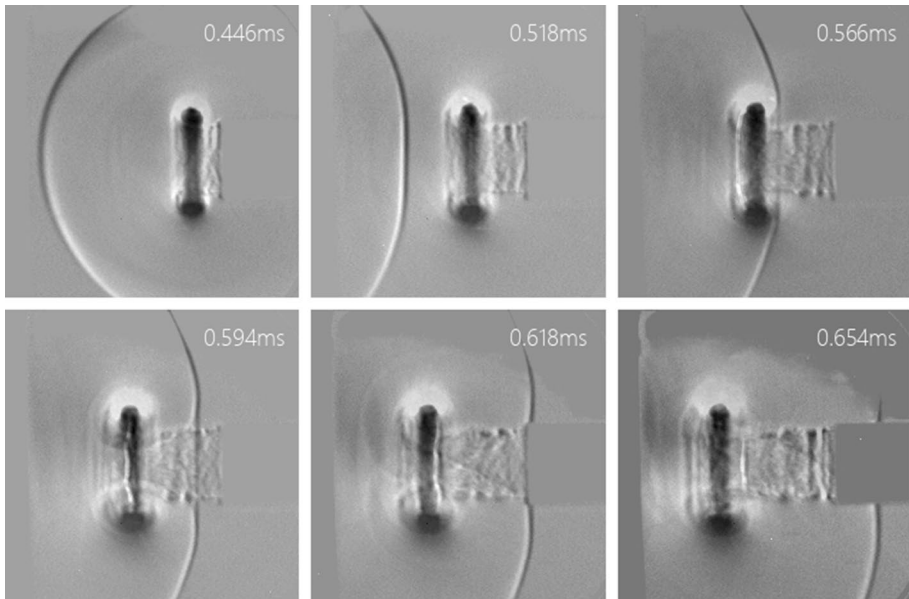


Fig. 6 Schlieren images of flat plate impingement with $p_1 = 0.928$ bar and $p_4/p_1 = 4.1$

Since the higher p_4/p_1 leads to a stronger shock wave and vortex structures, this shock wave strength reduction should be attributed to the decrease of the environmental pressure and the effect of p_4/p_1 on the shock Mach number is excluded automatically. Third, the intensity of the boundary of the vortex ring decreases in Figs. 4 and 5, compared with the vortex ring in Fig. 3. Fourth, the Kelvin–Helmholtz instability usually appears at the shear layer of the wake because of the mixing of the jet flow and the exterior gas, presenting clear vortex structures in ambient atmosphere, such as in the schlieren images in Ref. Kontis et al. (2006) and Fig. 3. However, these vortices, due to the instabilities, become vague. Unlike the vortex ring in ambient atmosphere, the vortex ring in reduced pressure environments expands rapidly, which subsequently forces the internal flow structures to grow. This growth in size will decrease the local pressure of the internal structures, resulting in difficulty in visualising them in schlieren images. This implies that if the environmental pressure is continuously decreased, vortex flow structures, such as CRVRs and vortices in the shear layer, will become difficult to observe and eventually disappear, which is consistent with the results found in previous work (Cao et al. 2021).

With the current experimental apparatus, it was not possible to capture any structures when the pressure in the vacuum chamber was lower than approximately 0.15 bar because the schlieren system used was not as sensitive as that for visualising sound waves (Hargather et al. 2010) and the shock wave and the vortex ring became too fast to be captured by the high-speed camera. Hence, we introduce the flat plate with a pressure transducer at its centre to conduct pressure measurements and identify the footprints of vortex rings when $p_1 < 0.1$ bar. The flow evolution changes once a surface blocks the propagation path. The whole process in atmosphere is shown in Fig. 6, where $p_4/p_1 = 4.1$, is similar to the schematic in Figure 2 of Ref. Mariani et al. (2013). The incident shock wave impinges on and is then reflected from the flat plate. The reflected shock wave is diffracted by the vortex core when it interacts with the vortex ring. Due to the rotation inside the vortex core, a toroidal shock wave forms (Mariani et al. 2013) at 0.594 ms and focuses at the centre at 0.618 ms.

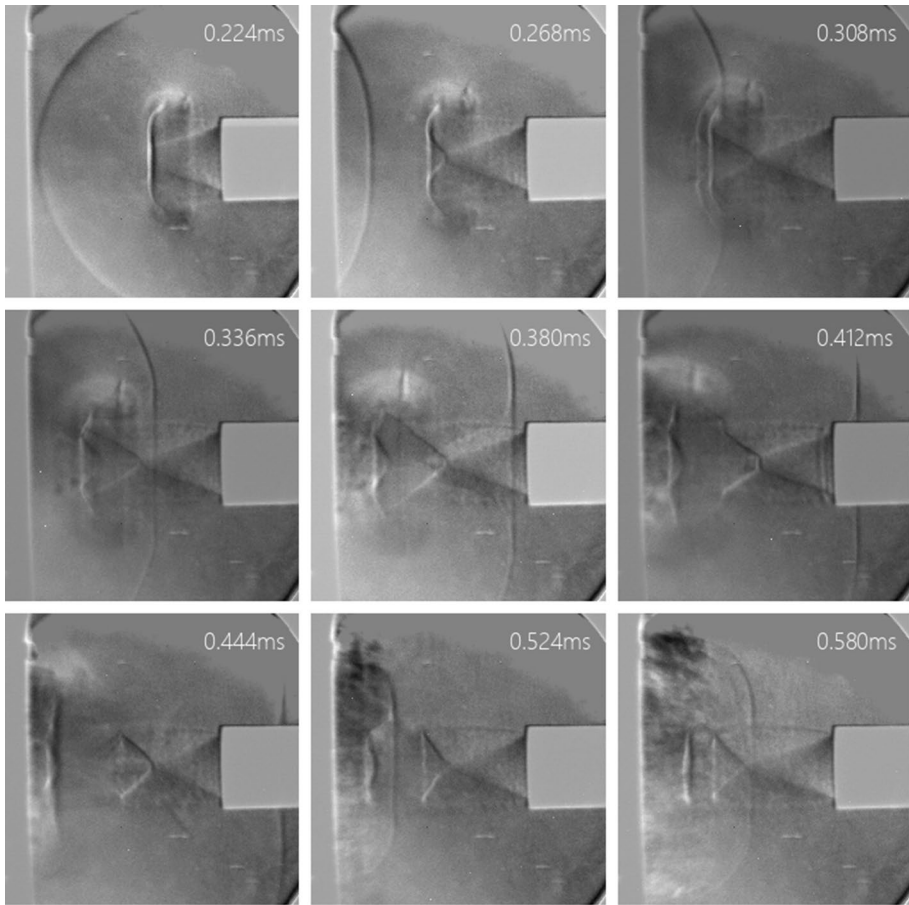


Fig. 7 Schlieren images of flat plate impingement with $p_1 = 0.228$ bar and $p_4/p_1 = 13.4$

The shock Mach number is relatively low in Fig. 6. Increasing the pressure ratio to $p_4/p_1 = 14.3$ by reducing p_1 to 0.228 bar leads to the formation of a CRVR and an embedded shock wave, as shown in Fig. 7. As described in Ref. Kontis et al. (2008), the reflected shock wave interacts with the vortex ring and turns into the shape of the embedded shock wave at 0.308 ms, and the CRVR becomes the first vortex ring to impinge on the surface, followed by the main vortex ring. Subsequently, a boundary layer forms and extends in the radial direction and the embedded shock wave inside the vortex ring is reflected from the surface (Mariani et al. 2013), as shown in Fig. 7 at 0.524 ms.

In Ref. Zare-Behtash et al. (2009), it has been found that the vortex ring diameter increases with the shock Mach number, which has also been found numerically (Cao et al. 2021). It can be observed that the vortex size increases slightly in Fig. 6, but the vortex ring size in Fig. 7 increases significantly at 0.224 ms and 0.38 ms. Thus, the vortex ring size increases as a result of both the increase in the shock Mach number and the reduction of the environmental pressure. Figure 8 shows the pressure signal from the transducer at the centre of the flat plate for the different background pressures. The normalised pressure distribution variation in Fig. 8a, particularly the increase in the slope of the primary shock

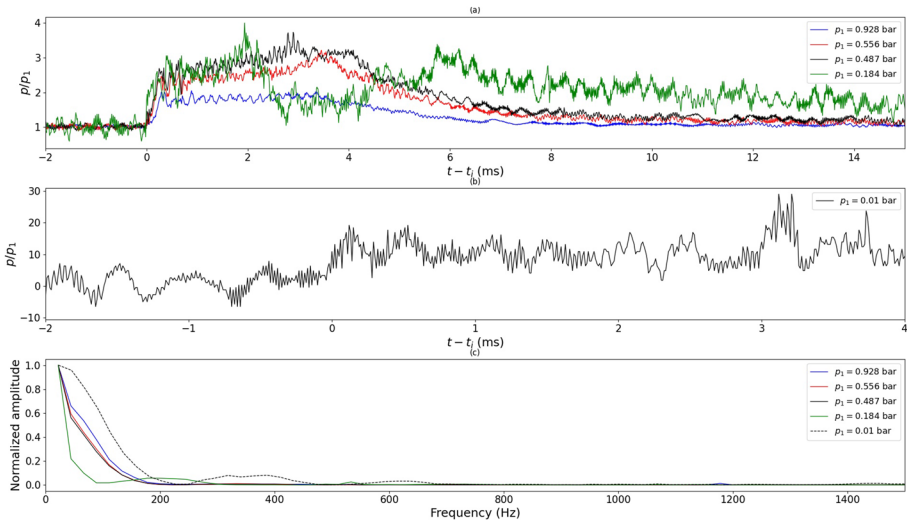


Fig. 8 **a, b:** Normalized pressure distribution with time at the center of the flat plate. t_i is the time that the pressure start to increase due to the shock wave. **c** Frequency distribution of the pressure signal using a fast Fourier transform

wave, indicates that the flow structure changes as the pressure ratio, p_4/p_1 , increases, such as the formation of the CRVRs and the embedded shocks. A similar trend when p_1 is equal to 0.556 bar and 0.487 bar shows the similar structure of the two cases, and the shock wave and the following vortex ring are still recognizable. Due to the limited resolution, the pressure signal is noisy when $p_1 < 0.1$ bar, and the primary shock wave is difficult to resolve, as shown in Fig. 8b. The $t - t_i$ is limited to 4 ms in Fig. 8b because there is an unnatural pressure surge and fluctuation due to impingement of the debris from the diaphragm.

Figures 6 and 7 show that the vortex ring impingement process is composed of the impingement of a series of characteristic flow structures, which will show a similar pressure signal frequency in the frequency domain. Figure 8c presents the normalised pressure signal in the frequency domain using a fast Fourier transform. The distribution of $p_1 = 0.556$ bar and $p_1 = 0.487$ bar are in excellent agreement, indicating the consistency of the basic flow structures during the impingement. The slight difference between the case of $p_1 = 1$ bar and that of $p_1 = 0.556$ bar is caused by the difference in the vortex ring structure due to the shock Mach number. The three cases prove that similar flow features will give an identical frequency profile. When the environmental pressure is lower than 0.2 bar, the pressure frequency profile changes. The frequency distribution with $p_1 = 0.01$ bar does not agree well with that with $p_1 = 0.184$ bar in the range of 0 to 1000 Hz, but they share the same wave profile, i.e. a steep gradient and a following hump. It has been confirmed above that the vortex ring is formed when p_1 is around 0.2 bar, the high similarity of the pressure frequency distribution between the case of $p_1 = 0.184$ bar and that of $p_1 = 0.01$ bar implies the existence of the vortex structure when p_1 is as low as 1.0 kPa.

5 Conclusions and Future Work

In this work, the vortex ring in a reduced pressure environment is investigated at a fundamental level to bridge the knowledge gap between the conventional vortex rings in ambient atmosphere and rarefied vortex rings. The schlieren imaging technique is used to visualise the jet flow from the shock tube inside a vacuum chamber. The increase in the thickness of the shock wave has been observed in reduced pressure conditions. The vortex flow structure degeneration phenomenon observed in previous numerical work has been experimentally proven. The strengths of the CRVRs and the vortices in the shear layer due to the Kelvin–Helmholtz instability decrease because of the reduction in environmental pressure. The CRVR sill can be found in a lower pressure environments as long as the pressure ratio reaches the critical value. The existence of the vortex ring when the environmental pressure is about 1.0 kPa is confirmed using the pressure signal in the frequency domain.

For future work, it is necessary to increase the sensitivity of the schlieren or use other optical methods to capture the vortex ring evolution process as the Knudsen number increases significantly. A more sensitive DAQ system can be used to collect pressure signals to study the existence of the vortex ring in the near transition flow regime. A plunger for breaking the diaphragm can be designed and added to improve the behaviour of the shock tube. The influence of the length of the driver section, the pressure ratio, and the geometry of the nozzle on the evolution of the vortex rings can be investigated.

Acknowledgements The authors are grateful to the technical staff, including Mr Alistair Macfarlane, Mr Thomas Dickson, and Mr Wilson MacDougall, at the University of Glasgow for their assistance in manufacturing and repairing the shock tube. Thanks to Dr Senthilkumar Subramanian and Ms Gaargi Jain for setting up the schlieren and providing assistance with the experiments.

Author Contributions ZC designed the experimental layout, conducted the experiments and the post-processing, and wrote the main manuscript text. KK, HH and CW supervised the research, provided guidance, reviewed and correct the manuscript. T-TC and MBA conducted the validations and experiments.

Funding This research received no funding.

Data Availability All of the material is owned by the authors and/or no permissions are required.

Declarations

Conflict of interest The authors have no competing interests as defined by Springer, or other interests that might be perceived to influence the results and/or discussion reported in this paper.

Ethical Approval This material is the authors' own original work, which has not been previously published elsewhere. The results/data/figures in this manuscript have not been published elsewhere, nor are they under consideration (from you or one of your Contributing Authors) by another publisher. I have read the Springer journal policies on author responsibilities and submit this manuscript in accordance with those policies.

Open Access This article is licensed under a Creative Commons Attribution 4.0 International License, which permits use, sharing, adaptation, distribution and reproduction in any medium or format, as long as you give appropriate credit to the original author(s) and the source, provide a link to the Creative Commons licence, and indicate if changes were made. The images or other third party material in this article are included in the article's Creative Commons licence, unless indicated otherwise in a credit line to the material. If material is not included in the article's Creative Commons licence and your intended use is not permitted by statutory regulation or exceeds the permitted use, you will need to obtain permission directly from the copyright holder. To view a copy of this licence, visit <http://creativecommons.org/licenses/by/4.0/>.

References

- Anderson, J.D.: Modern Compressible Flow: With Historical Perspective, vol. 12. McGraw-Hill, New York (1990)
- Baird, J.: Supersonic vortex rings. Proc. R. Soc. Lond. A Math. Phys. Sci. **409**(1836), 59–65 (1987)
- Bradley, J.N.: Shock Waves in Chemistry and Physics, p. 111. Methuen & Co.Ltd, London (1963)
- Brouillette, M., Hebert, C.: Propagation and interaction of shock-generated vortices. Fluid Dyn. Res. **21**(3), 159–169 (1997)
- Cao, Z., White, C., Kontis, K.: Numerical investigation of rarefied vortex loop formation due to shock wave diffraction with the use of roticity. Phys. Fluids **33**(6), 067112 (2021)
- Dora, C., Murugan, T., De, S., Das, D.: Role of slipstream instability in formation of counter-rotating vortex rings ahead of a compressible vortex ring. J. Fluid Mech. **753**, 29–48 (2014)
- Elder, F., Jr., De Haas, N.: Experimental study of the formation of a vortex ring at the open end of a cylindrical shock tube. J. Appl. Phys. **23**(10), 1065–1069 (1952)
- Hargather, M.J., Settles, G.S., Madalis, M.J.: Schlieren imaging of loud sounds and weak shock waves in air near the limit of visibility. Shock Waves **20**(1), 9–17 (2010)
- Hillier, R.: Computation of shock wave diffraction at a ninety degrees convex edge. Shock Waves **1**(2), 89–98 (1991)
- Kontis, K., An, R., Edwards, J.A.: Compressible vortex-ring interaction studies with a number of generic body configurations. AIAA J. **44**(12), 2962–2978 (2006)
- Kontis, K., An, R., Zare-Behtash, H., Kounadis, D.: Head-on collision of shock wave induced vortices with solid and perforated walls. Phys. Fluids **20**(1), 016104 (2008)
- Li, G.: Experimental studies on shock wave interactions with flexible surfaces and development of flow diagnostic tools. PhD thesis, University of Glasgow (2020)
- Li, G., Ukai, T., Kontis, K.: Characterization of a novel open-ended shock tube facility based on detonation transmission tubing. Aerosp. Sci. Technol. **94**, 105388 (2019)
- Mariani, R., Kontis, K., Gongora-Orozco, N.: Head on collisions of compressible vortex rings on a smooth solid surface. Shock Waves **23**(4), 381–398 (2013)
- Martinez, J., Worthy, E.: International space station (ISS) thruster plume contamination and erosion control for visiting spacecraft. Microsc. Microanal. 1–3 (2020)
- Murugan, T., De, S., Dora, C., Das, D.: Numerical simulation and PIV study of compressible vortex ring evolution. Shock Waves **22**(1), 69–83 (2012)
- Poudel, S., Chandrala, L., Das, D., De, A.: Characteristics of shock tube generated compressible vortex rings at very high shock Mach numbers. Phys. Fluids **33**(9), 096105 (2021)
- Qin, L., Xiang, Y., Lin, H., Liu, H.: Formation and dynamics of compressible vortex rings generated by a shock tube. Exp. Fluids **61**(3), 86 (2020)
- Thangadurai, M., Das, D.: Characteristics of counter-rotating vortex rings formed ahead of a compressible vortex ring. Exp. Fluids **49**(6), 1247–1261 (2010)
- White, C., Zare-Behtash, H., Kontis, K., Ukai, T., Merrifield, J., Evans, D., Coxhill, I., Langener, T., Van den Eynde, J.: Test Facility to Investigate Plume-Regolith Interactions (2019)
- Xiang, Y., Qin, L., Qin, S., Liu, H.: Circulation production model and unified formation number of compressible vortex rings generated by a shock tube. Phys. Fluids **35**(3), 036121 (2023)
- Zare-Behtash, H., Kontis, K., Gongora-Orozco, N.: Experimental investigations of compressible vortex loops. Phys. Fluids **20**(12), 126105 (2008)
- Zare-Behtash, H., Kontis, K., Gongora-Orozco, N., Takayama, K.: Compressible vortex loops: effect of nozzle geometry. Int. J. Heat Fluid Flow **30**(3), 561–576 (2009)
- Zhang, H., Chen, Z., Li, B., Jiang, X.: The secondary vortex rings of a supersonic underexpanded circular jet with low pressure ratio. Eur. J. Mech.-B/Fluids **46**, 172–180 (2014)